Scientific Reports

https://doi.org/10.1038/s41598-026-43781-5

Article in Press

Enhancing safety and early warning capabilities in mining through microseismic monitoring technology

Received: 1 February 2026

Accepted: 6 March 2026

Published online: 17 March 2026

Cite this article as: Jin J., Xiao Y., Wu P. *et al.* Enhancing safety and early warning capabilities in mining through microseismic monitoring technology. *Sci Rep* (2026). https://doi.org/10.1038/s41598-026-43781-5

Jiaxu Jin, Yong Xiao, Pengfei Wu, Jun Wang, Jie Liu, Yunlong Mo & Lei Zhang

Enhancing Safety and Early Warning Capabilities in Mining through Microseismic Monitoring Technology

Jiaxu Jin [a], Yong Xiao [a], Pengfei Wu [a], Jun Wang [b*], Jie Liu [c], Yunlong Mo [d,e], Lei Zhang [f]

[a] School of Civil Engineering, Liaoning Technical University, Fuxin. Liaoning, 123000, China

[b] State Key Laboratory of Deep Earth Engineering Intelligent Construction and Healthy Operation and Maintenance, Shenzhen University, Shenzhen. Guangdong, 518060, China

[c] Northeastern University, Shenyang. Liaoning, 110819, China

[d] China Coal Research Institute, Beijing 100013, China

[e] State Key Laboratory of Coal Mine Disaster Prevention and Control, Beijing 100013, China

[f] Machinery Technology Development Co., Ltd. Beijing, 100190, China

[*]Corresponding author's E-mail address: 18287857533@163.com (J. Wang)

Abstract

In the mining industry, microseismic monitoring has emerged as a crucial instrument for reducing risks related to the stability of underground rock masses. The present research conducts an analysis of dynamic hazards specifically at the 8204-2 working face in Tashan Mine. A novel monitoring framework is introduced, which integrates a nonlinear threshold curve model with a wireless microseismic monitoring system. The results demonstrate the effectiveness of the microseismic monitoring system with high-frequency sampling, utilizing the nonlinear threshold model, in detecting and providing real-time early warnings for microseismic signals, even in challenging geological environments. Practical implementation and monitoring over the past six months revealed that the microseismic monitoring system, employing the threshold curve model, achieved a monitoring and early warning accuracy exceeding 95%. This model combines the construction

of a nonlinear threshold curve with dynamic conversion of confidence factors, and implements multi-level graded early warning based on the matching degree between real-time data and the hazard model, making its accuracy superior to traditional monitoring and early warning systems. Consequently, this study holds great significance in enhancing precise identification and early warning capabilities for mine microseism, as well as improving safety assessments for deep rock mining and construction practices.

Keywords: Deep mine; Dynamic disaster; Microseismic monitoring; Early warning

1 Introduction

As underground mining operations extend spatially and progress to greater depths, microseismic events in mines have grown notably more frequent[1-5]. Such events are often initiated by excessive vibrational energy released within mining zones. The classification of microseismic activities in mines plays a crucial role in mine accident management and post-disaster recovery. As microseismic monitoring systems have become widely adopted, they have generated substantial volumes of time-sequential microseismic data. Traditional time-sequential data, being directly linked to time, has the potential to reveal inherent data characteristics and patterns.

Recent years have witnessed extensive investigation into microseismic monitoring methodologies. As an illustration, Cui et al.[6] utilized this technology to surveil and forewarn tunnel rock bursts, thereby evidencing its efficacy in both monitoring and early alerting[7-14]. However, owing to the unpredictable, complex, attenuating, and diffusing nature of microseismic time series data[15], coupled with the diverse underground rock structures and complex mining environments, the identification of microseismic time series has become a formidable challenge. Consequently, research on the identification of microseismic signals has expanded significantly[16-20]. Jiang et al.[16] explored the recognition algorithm for microseismic signals by means of wavelet analysis (WA), and their findings

demonstrated that WA possesses high efficiency and accuracy in the denoising and reconstruction of mine microseismic signals. Nevertheless, inherent defects of the threshold function or improper selection of wavelet functions in WA can significantly affect the denoising results.Recent research on nonlinear threshold models for microseismic monitoring has made progress—Zhang et al.[21] revealed the nonlinear evolution characteristics of acoustic emission event networks and established a multifractal early warning model, providing a theoretical basis for the nonlinear analysis of seismic signals in geotechnical engineering. However, this model either lacks dynamic threshold adjustment for mining disturbances or fails to be effectively applied in soft rock working faces and deep coal mines with severe stress concentration, and it is rarely integrated with wireless monitoring systems to form a complete engineering early warning framework.

In the context of early warning systems for dynamic hazards, He et al.[22] employed the AE-EMR method for coal mine dynamic hazard early warning. This method not only established a theoretical foundation but also played a pivotal role in effectively reducing the frequency of underreported accidents and ensuring safety[23]. Microseismic monitoring and early warning technology have the capability to detect microseismic events occurring during stress enhancement and inelastic deformation stages. Based on a systematic assessment of the concentration patterns and source parameters of a multitude of microseismic signals, successful predictions of rock bursts at the failure stage were achieved[24-26]. These predictions, in turn, offered essential theoretical support for monitoring and early warning technologies.

Upon entering deep mining operations, it becomes evident that the characteristics of deep coal and rock undergo significant transformations, leading to distinct variations in the mechanisms causing disasters and the criteria for identifying deep dynamic hazards in coal mines[27]. Presently, most of the existing monitoring systems are deployed underground. However, the harsh underground

environment poses challenges, such as potential instrument instability and compromised monitoring signal quality. Additionally, the high cost associated with these monitoring systems hinders the establishment of high-density measurement points, resulting in numerous monitoring blind spots within the underground area[28]. In the context of deep mining, the transmission of monitoring data from top to bottom typically relies on wired connections, which are challenging to install and susceptible to damage. This situation is not conducive to early disaster warning. Moreover, the large size of monitoring stations and the fixed positioning of sensors do not allow for flexible optimization of layouts in sync with the shifting mining areas. Regrettably, these issues have proven difficult to surmount, resulting in diminished early warning accuracy. Consequently, there is an urgent need to explore new research methods to address these challenges.

In this study, we center on the microseismic surveillance technology applied to the dynamic hazard of the 8204-2 working face in the Tashan mining site, which is characterized by the presence of soft rock in the advancing face and a high concentration of stress in the coal pillars between adjacent working faces.It tackles the existing challenges posed by high-frequency dynamic microseismic hazards and inadequate early warning accuracy in coal mining operations. To improve the effectiveness and accuracy of monitoring and early warning for mine microearthquakes, We present a new approach built upon the construction of a nonlinear threshold curve model. By utilizing a high-frequency microseismic monitoring system, we employ a linear regression approach to analyze historical hazard data and establish a microseismic hazard event model. This model enables us to explore future trends in dynamic hazard occurrences and develop effective risk warning methods. Ultimately, our research aims to provide essential support for advanced warning and preventive measures against complex dynamic hazards in deep mines.

2 Microseismic signal localization and recognition calculation method

The dynamic hazards in coal mines arise from the mechanical characteristics of the soft rock advancing face within the deep coal seam, making them susceptible to external forces. The mechanical changes within the soft coal seam often transmit information through micro-seismic waves. However, the identification and accurate location of these micro-seismic signals present unprecedented challenges owing to the intricate and ever-changing geological environment found in deep coal seams. Shi et al. addressed this issue by improving the precision of P-wave identification in underground microseismic waveforms through the utilization of the dual filtering algorithm[29].

In deep coal mines, it is possible for small microearthquakes to occur even in the absence of a microseismic event, further complicating the situation. By employing the identification of microseismic waveform images, it becomes possible to provide highly precise microseismic data to a significant extent, thus enhancing the understanding of the microseismic activity[30].

2.1 Arrival time and position calculation of microseismic signals

The high-frequency microseismic surveillance and pre-warning system is utilized for monitoring mining areas. It determines the vibration waveform corresponding to the real-time vibration signal based on the gathered microseismic waveform and determines the characteristic information of the background noise in the real-time vibration waveform signal. Using this background noise characteristic information, the real-time vibration waveform signal is processed to isolate the effective microseismic waveform signal.

When activated, the termination point of the short time window, denoted as ti, for each monitoring sub-station is recorded. The 5-second amplitude data of each sensor before and after this time are stored. The coordinates of each sensor within a signal are denoted as $(x_1, y_1, z_1) \ldots (x_n, y_n, z_n)$, and the average amplitudes of the long and short time windows, denoted as A_{long} A_{short}, are calculated according to

formulas (1) and (2).

$$\overline{A_{short(i)}} = \frac{1}{N_2} \sum_{i=1}^{N_2} \left| A_{(i)} \right| \tag{1}$$

$$\overline{A_{long(i)}} = \frac{1}{N_1} \sum_{i=1}^{N_1} \left| A_{(i)} \right| \tag{2}$$

Where, $A_{(i)}$ is the average count of i channels in the normalized Data. N_1: the count of sampling points contained in 50 ms, i.e. the count of points contained in the long time window. N_2: the count of sampling points contained in 10 ms. The space vector $A_{(i)}$ was projected in the x, y, z coordinate directions, and the modulus value of $A_{(i)}$ is substituted into the calculation, which is shown in formula (3).

$$\left| \vec{A}_{(i)} \right| = \sqrt{x^2 + y^2 + z^2} \tag{3}$$

If there are k activated sensors, then there are C_k^5 possible permutations and combinations to calculate the source coordinates, the formula is as follows:

$$\begin{aligned} &\sqrt{(x_1\text{-x})^2 + (y_1\text{-y})^2 + (z_1\text{-z})^2} - C(t_1 - t) = 0 \\ &\text{L L L L L L L L L} \\ &\sqrt{(x_5\text{-x})^2 + (y_5\text{-y})^2 + (z_5\text{-z})^2} - C(t_5 - t) = 0 \end{aligned} \tag{4}$$

Where, x_i, y_i and z_i represent the components of the microseismic perceived data of channel i in the directions of the X-, Y-, and Z-axes, individually, and t_i denotes the time. According to the above equations, (x_i, y_i, z_i, t_i) is obtained, and the permutation and combination calculation of C_k^5 is carried out by using multi-parameter characteristics to obtain the average value. The obtained coordinate (x, y, z, t) is the source coordinate of microseismic event.

2.2 Identification of Microseismic Signals for Coal Mine Dynamic Hazards

The wavelet analysis (WA) technique is an effective tool for analyzing nonstationary and nonlinear signals[31]. It allows for multi-resolution analysis, enabling precise localization in the time and frequency domains. By utilizing wavelet transform, microseismic signals, along with other non-stationary signals, can be analyzed and processed effectively[15, 16]. The wavelet's waveform bears a striking resemblance to that of a microseismic signal, making it possible to adjust

wavelet parameters during the transformation process to achieve denoising effects. Formula (5) represents the wavelet transform formula, assuming that denotes the pure original signal, represents the noise signal, represents the additive noise, and k signifies the noise intensity, $f(t)=(f_1, f_2,..., f_n)$ is the pure original signal, $X(t)=(x_1, x_2,..., x_n)$ is the background noise signal, $e(t)$ is the additive noise, and k is the intensity of background noise.

$$X(t)=f(t)+k' e(t) \tag{5}$$

Where, $f(t)$ is the raw original low-frequency signal, and $X(t)$ is the non-stationary high-frequency noise signal. In the process of wavelet decomposition and denoising, the wavelet basis function with good adaptability and a decomposition level of 154 need to be adopted for signal processing, which is determined based on the 10 kHz high sampling frequency of the monitoring system, the dominant frequency range of mine microseismic signals and the high-frequency random noise interference in the mining area, and the corresponding wavelet coefficients can be obtained by multi-scale decomposition of the signal. Then the appropriate threshold function and thresholds are selected to quantify the wavelet coefficients at each scale. Finally, the lowest frequency coefficient of the bottom layer and the high frequency coefficient of each layer are reconstructed to gain the denoised microseismic waveform, as illustrated in Fig. 1.

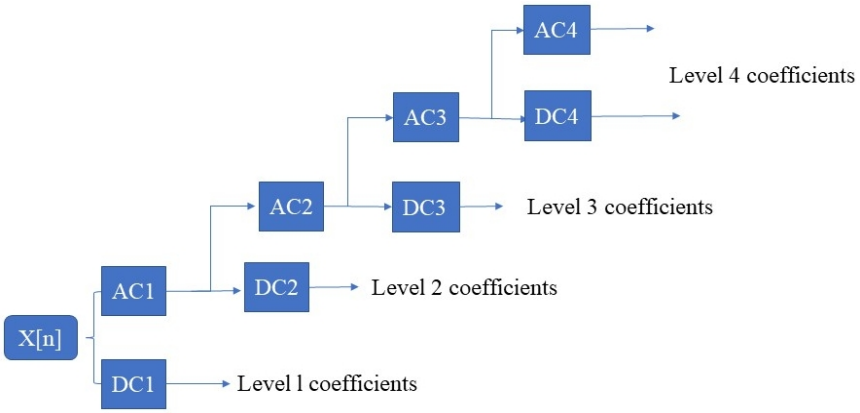

Fig. 1 Wavelet decomposition process diagram.

Fig. 1 shows the process of wavelet decomposition, where $X[n]$ is represented as the microseismic temporal sequence data, $DC1$ and $AC1$ are the

decomposition detail and approximation coefficients of first-layer wavelet, respectively[15].In order to solve the flaws of the existing soft threshold and hard threshold, this paper proposed a new function of threshold as formula (6).

$$W'_{j,k} = \begin{cases} sign(W_{j,k}) \cdot \left(|W_{j,k}| - \dfrac{\lambda^{k_1+1}}{|W_{j,k}|^{k_1}} \right) & |W_{j,k}| \geq \lambda \\ sign(W_{j,k}) \cdot \left(W_{j,k} - \left(1 - \dfrac{e^{k_2}-1}{e^{k_2}+1} \right) \lambda \right) & |W_{j,k}| < \lambda \end{cases} \tag{6}$$

Where, k_1 and k_2 are coordination factors (k_1 and k_2 are positive), λ is the selected threshold, $w_{j,k}$is the unprocessed wavelet coefficient, and $\dot{w}_{j,k}$ is the acquired wavelet coefficient by processing the function of threshold. Since noise usually appears in the high frequency coefficients of wavelet decomposition, the processed wavelet coefficients are for the high-frequency signal components.

After performing wavelet decomposition, the next step involves the inverse transform of wavelet coefficients, resulting in the reconstruction of a denoised signal. In the above figure, the default number of decomposition layers is defined as 4. Following this, the approximation coefficient and detail coefficients, which have been processed by a threshold function at the lowest level, are employed for one-dimensional wavelet reconstruction, resulting in the generation of a single layer of reconstructed signal. This process is repeated, reconstructing the approximation and detail coefficients layer by layer until an approximate original signal is obtained.

Extreme Learning Machine (ELM) is a machine learning algorithm specifically designed for the efficient training of single-hidden-layer feed-forward neural networks (SLFNs)[32]. In this method, random generation is adopted for the connection weights between the 182-node input layer and the hidden layer of the ELM model. During operation, only the unique optimal solution can be obtained by solely determining the number of hidden layer nodes. Supposing that there are N distinct samples (x_i, y_i) and $x_j = [x_{j1}, x_{j2}, ..., x_{jn}]^T$, $y_j = [y_{j1}, y_{j2}, ..., y_{jm}]^T \in R^m$. A single-

layer hidden architecture feed-forward neural network with K hidden nodes and activation function $g(x)$ can be represented as formula (7).

$$\sum_{j=1}^{K} b_i \times g(w_j \times X_j + b_j) = O_i, i = 1, \ldots, N \tag{7}$$

Where, $w_j = [w_{j1}, w_{j2}, \ldots, w_{jn}]^T$ denotes the connection weight between the node of the input layer and the node of hidden layer j. $b_j = [b_{j1}, b_{j2}, \ldots, b_{jm}]^T$ is the connection weight between hidden layer node j and the output layer; w is the bias of neurons in layer j of the hidden layer; $w_j \times X_j$ is internal product; $O_j = [O_{j1}, O_{j2}, \ldots, O_{jn}]^T$ is the output value. To ensure the accuracy of experimental results and make them more consistent with actual samples, $\sum_{j=1}^{K} \| O_i - y_i \| = 0$ should be set.

3 Nonlinear microseismic monitoring and early warning model

3.1 The establishment of a microseismic disaster early warning model

This study employs linear regression to analyze historical microseismic disaster data, normalizing and gridifying the original nonlinear time series to extract feature points with clear physical significance, thereby filtering out randomness and highlighting local linear features. This method is suitable for mining areas where coal seam occurrence is stable and microseismic events induced by mining are the main type, but it is not applicable to areas with structural plane development and complex disturbance factors of microseismic events.

The waveform regression equation is constructed to enable the visualization of microseismic signals in colliery and facilitate the realization of dynamic disaster risk warnings. The normalization method is employed to preprocess a significant amount of historical data related to dynamic disaster events in coal mines. By transforming the microseismic signal data to a consistent interval, a series of sequentially accumulated perceptual data points are obtained. Fig. 2 illustrates the schematic diagram depicting the division of the historical dataset into local

sensing datasets after data gridding.

During the feature extraction process of mine hazard event data, it is assumed that the eigen points, representing the characteristics of the local data throughout the entire event data range, are known. To quantify the impact of eigen points on the perceived coal mine signal data, the concept of tight support is introduced, allowing for the establishment of a weight support domain[15]. Consequently, after the gridding process, the influence range of a specific point X is determined, and a circle with a radius denoted as $r=(\max(x_i)-\min(x_i))*2/10$ is selected as the weight function's support domain. Next, the coal mine signal data contained within the influence area of the reference point X is identified. When solving for eigen points, the mutual influence of the coal mine signal data points from the surrounding hazard events is taken into consideration.

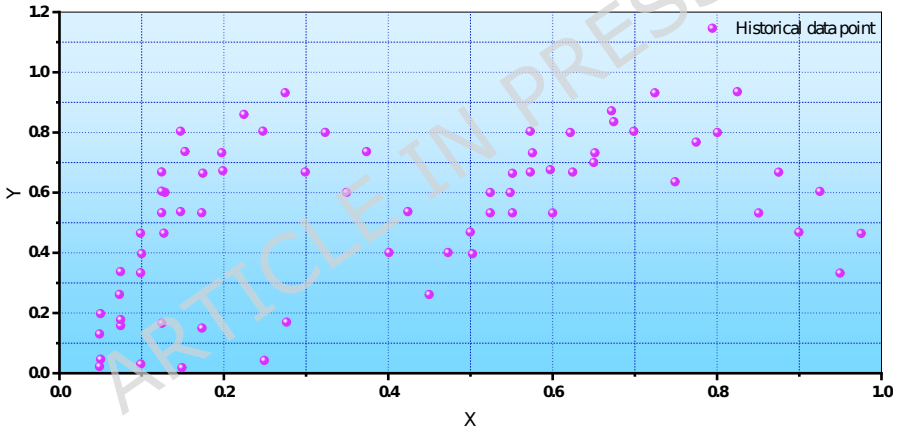

Fig. 2 The schematic diagram illustrating the standardization process of historical hazard events after conducting data gridding.

After determining the influence range of the coal mine signal and identifying the perceived data points (reference points) within this range, it is crucial to establish a weight function that measures the degree of influence of reference points on standard points. In the study, cubic spline function was selected as the weight function, denoted $s\phi=x-x_i\ s=s\phi/r$, as shown in formula (8).

$$w(s)=\begin{cases}\frac{2}{3}-4s^2+4s^3 & s\le\frac{1}{2}\\ \frac{4}{3}-4s+4s^2-\frac{4}{3}s^3 & \frac{1}{2}<s\le 1\\ 0 & s>1.\end{cases} \tag{8}$$

In the equation, $x-x_i$ represents the distance from the reference point to the standard point in the coal mine signal, while r denotes the influence radius. The parameter s is the input parameter for the weight function.

Within each grid, the influence area of the standard points is initially determined. Subsequently, the perceived data points within this area are obtained, and the eigen point values are calculated based on the equation. The mobile regression method determines the eigen point value at a specific standard point, denoted as χ, using a coefficient vector and a basis function.

$$f(x)=\sum_{i=1}^{m} p_i(x)a_i(x)=p^T(x)a(x) \tag{9}$$

Where, $a(x)=(a_1(x), a_2(x),\cdots, a_m(x))^T$ is the undetermined factor, m is the count of fundamental functions, and $p(x)=(p_1(x), p_2(x),\cdots, p_m(x))^T$ is the vector of fundamental functions. With the aim of achieving a more accurate local approximation, It is imperative to reduce the weighted square sum of the differences between local approximations $f(x_i)$ and the perceived data value y_i to a minimum. Accordingly, the discrete weighted L_2 paradigm for residual analysis is:

$$J=\sum_{i=1}^{n} w(x-x_i)[f(x)-y_i]^2=\sum_{i=1}^{n} w(x-x_i)[p^T(x_i)a(x)-y_i]^2 \tag{10}$$

Where, n is the count of perceived data in the local area, $f(x)$ is the local fitting function, and $w(x-x_i)$ represents the weight support function value of the node x_i. After getting the undetermined coefficient $a(x)$ of the local fitting function, the minimum value of J was obtained, and formula (10) can be expressed in a matrix form:

$$J=(Pa(x)-Y)^T W(x)(Pa(x)-Y)$$

The matrix P with $Y=(y_1, y_2, \cdots, y_n)^T, W(x)=diag(w_1(x), w_2(x), \cdots, w_n(x))$ $w_i(x)=w(x-x_i)$ can be represented in the following form:

$$P=\begin{bmatrix} p_1(x_1) & p_2(x_1) & \cdots & p_m(x_1) \\ p_1(x_2) & p_2(x_2) & \cdots & p_m(x_2) \\ \vdots & \vdots & \ddots & \vdots \\ p_1(x_n) & p_2(x_n) & \cdots & p_m(x_n) \end{bmatrix}$$

According to the regression principle, the undetermined coefficient was obtained as follows:

$$a(x)=A^{-1}(x)B(x)Y$$

Where, $A(x)=P^T W(x)P, B(x)=P^T W(x)$, the fitting function (approximate function) was obtained by substituting it into formula (10)

$$f(x)=\sum_{i=1}^{n} f_i^k(x)y_i=y^k(x)Y$$

Where, $y^k(x)$ is the shape function and k is the order of the basis function.

$$y^k(x)=[f_1^k, f_2^k, \cdots, f_n^k]=p^T(x)A^{-1}(x)B(x)$$

According to the equation, the coefficient matrix $a(x)$ was obtained, and the eigen point value y_{ti} was further obtained. The y value of standard point x was calculated by cyclic calculation for each grid, and corresponding eigen data points (x_{ti}, y_{ti}) were obtained and stored, as shown in Fig. 3.

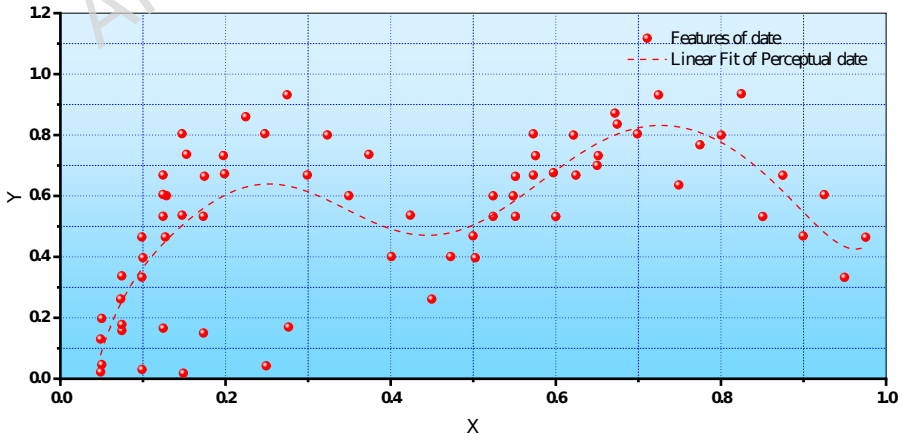

Fig. 3 Schematic diagram of data features.

The features of perceived data during the time period when hazard events occur are polynomial equations, which can hardly be represented by existing standardized equations, and there is no fixed mapping relationship between

hazard event data at the same time. Therefore, this paper proposed to find the curve function of hazard events by regression method, and achieve the representation for the trend of hazard events by polynomial equations by establishing a regression formula by regression theory. The form of regression equation was set as shown in formula (11). Firstly, N eigen points (x_i, y_i) were preprocessed, where $i=1,2,3....N$, $x_i = x_{ti}, y_i = y_{ti}$. For the convenience of calculation, the value of x_i was processed as follows:

$$x_i^{'} = x_i - \bar{x}$$

Where, $\bar{x} = \sum_{i=1}^{N} x_i / N$, then the regression equation of the hazard event is:

$$y_k^{'}(x,a) = a_0 + a_1(x - \bar{x}) + a_2(x - \bar{x})^2 + a_3(x - \bar{x})^3 + ... + a_m(x - \bar{x})^k$$

At this time, this expression is the curve equation of the hazard event, k denotes the maximum order of the polynomial equation, where $k \le n$ and $k \le 20$.

For the sake of calculation, let $x = x - \bar{x}$, then the formula becomes

$$y(x,a) = a_0 + a_1 x + L + a_k x^k \tag{11}$$

Where the ordinate y represents the value of historical perceived data, the abscissa x represents the relative time of hazard events, and k is the order of the formula. The aggregate of the squared deviations of the distances among each observed data point and the regression curve is expressed in formula (12).

$$R^2 \equiv \sum_{i=1}^{n} \left[y_i - y(x_i, a) \right]^2 \tag{12}$$

According to the regression theory, the regression equation needs to meet the minimum sum of the distance between data points of each hazard event and the regression curve, that is, the partial derivative of a_i in formula (12) is solved, simplified and expressed in a matrix form, as shown in formula (13).

$$\begin{bmatrix} n & \sum_{i=1}^{n} x_i & L & \sum_{i=1}^{n} x_i^k \\ \sum_{i=1}^{n} x_i & \sum_{i=1}^{n} x_i^2 & L & \sum_{i=1}^{n} x_i^{k+1} \\ M & M & O & M \\ \sum_{i=1}^{n} x_i^k & \sum_{i=1}^{n} x_i^{k+1} & L & \sum_{i=1}^{n} x_i^{2k} \end{bmatrix} \begin{bmatrix} a_0 \\ a_1 \\ M \\ a_k \end{bmatrix} = \begin{bmatrix} \sum_{i=1}^{n} y_i \\ \sum_{i=1}^{n} x_i y_i \\ M \\ \sum_{i=1}^{n} x_i^k y_i \end{bmatrix} \tag{13}$$

When the coefficient matrix a_i was solved, the regression equation was obtained, and the hazard event model was determined. As illustrated in Fig. 4, the X-axis is time, the Y-axis is hazard event perceived data, the order $k = 9$, that is, the model fitting degree is $k = 9$. The hazard event model can accurately describe the function relationship of perceived data over time.

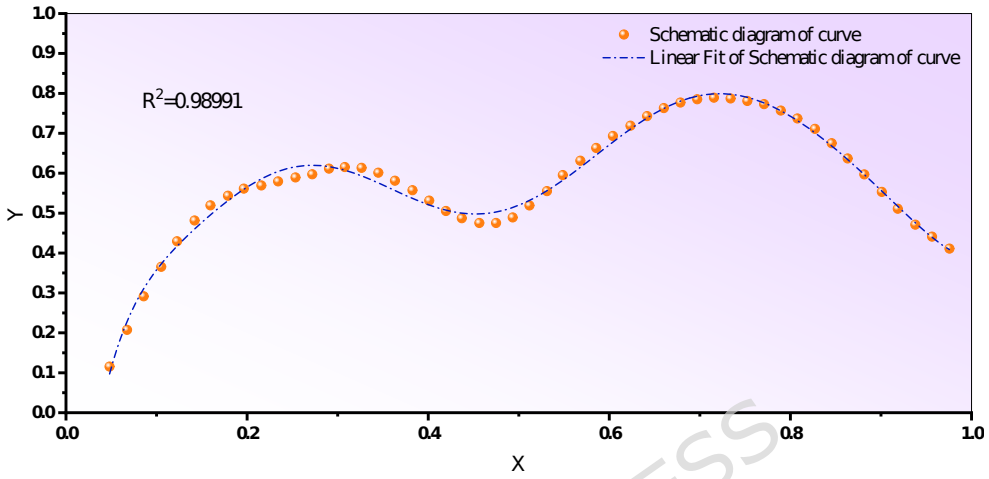

Fig. 4 Schematic diagram of curve fitting hazard event model Ω.

3.2 Early warning of coal mine dynamic hazard

According to Fig. 4, the hazard model Ω was fitted, and its equation was set as: $y(x,w) = w_0 + w_1 x + \cdots + w_M x^k$ then $y(x,w) = w_0 + w_1 x + \cdots + w_M x^k = \sum_{j=0}^{k} w_j x^j$ was a polynomial equation approximating the dynamic hazard curve. The deviation across the model Ω and the actual discrete observed data points is defined as the aggregate of squared euclidean distances from each individual discrete point to the model Ω. The error function $E(w)$ was supposed as shown in formula (14).

$$E(w) = \frac{1}{2}\sum_{n=1}^{N}\{y(x_n, w) - t_n\}^2 \tag{14}$$

Where, w is the coefficient vector of the regression formula, the actual perceived data of the parameter, x_n is the abscissa value of the n point in the data set, t_n is the ordinate value of x_n, and (t_n, x_n) is the observed value. The confidence interval of the model was established through the error function. Fig. 5 shows the diagrammatic sketch of the confidence interval.

As illustrated in Fig. 5, the confidence interval range was obtained by shifting

the regression model up and down with $\sqrt{E(w)}+q$, where, θ is the correction parameter, and more than 95% of the perceived data points fell within the confidence interval. At this time, when the real-time microseismic perceived data fell within the confidence interval, it was considered to meet the warning condition and trigger the risk warning. When rock burst disaster occurred, 98% of the perceived data fell within the confidence interval range of the template. Therefore, in the early warning stage, if the observed data fall within the range of confidence interval, it means that rock burst disaster may occur, but it does not necessarily happen, just indicating that there is a trend of rock burst disaster. For the purpose of measuring the degree of the trend of rockburst, a confidence factor transformation strategy was adopted.

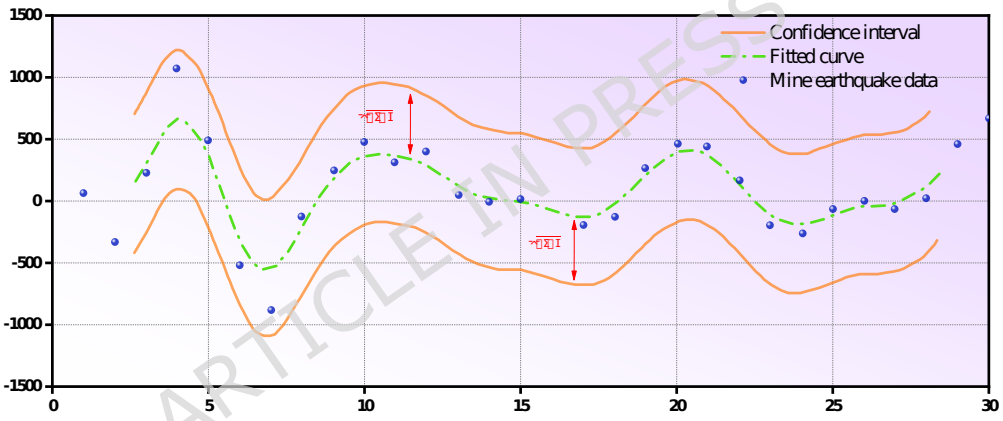

Fig. 5 Schematic diagram of confidence intervals.

For the purpose of removing the influence of mutation data on model matching, the method of shifting $1/2(g-x)$ unit was adopted, which can not only ensure that dangerous data can trigger early warning in time, but also reduce the impact of mutation data. The confidence interval represents an early warning range, and the perceived data within the confidence interval belong to dangerous data. According to the rules of hazard model establishment, the closer the data points are to the curve model, the higher the risk degree. Therefore, the concept of confidence factor was proposed in this paper. Confidence factor: an interval range that dynamically changes in real time with perceived data trend in the confidence

interval. Through the transformation of the confidence factor, the trend of the approximation between the perceived microseismic data and the curve model are described. When the fitting degree of the perceived data to the model was higher, the confidence factor was closer to the model; otherwise, the confidence factor was closer to the boundary of the confidence interval.

As shown in Fig. 6, ξ represents the confidence interval and γ represents the confidence factor. In the confidence interval range of model Ω, the initial value of γ was set as the range region of 1 / 2 $|\xi - \Omega|$ on both sides of model Ω, and γ was shifted up and down with the perception data close to or away from model Ω for trend prediction. When the microseismic perceived data stream was coming, the data were matched in real time. Taking the confidence interval below the model Ω as an example, a warning semaphore was set as the monitoring warning status marker, and the initial value was set to 0.

Confidence factor transformation rules:

① If n consecutive perceptual data points fall within the confidence interval but lie outside the confidence factor curve, the confidence factor curve is shifted outward by alpha units, and the monitoring process continues. If subsequent perceptual data points fall within the range of the confidence factor curve, the system prepares to enter the alert state and sets the warning signal quantity to 1. If the data points do not fall within the curve range, the confidence factor curve continues to shift outward by alpha units until the system enters the warning state. Once in the warning state, the confidence factor returns to its original position, and the warning signal quantity is set to 0.

② If n consecutive perceptual data points fall within both the range of the confidence interval and the range of the confidence factor curve, the confidence factor curve is shifted inward by alpha units to continue the monitoring process. If subsequent perceptual data points also fall within the range of the confidence factor curve, the warning semaphore is set to 1, indicating the system is ready to

enter the warning state. If the data points do not fall within the curve range, proceed to rule 1.

③ In the warning state, if n consecutive perceptual data points deviate from the confidence interval, the warning state is canceled, the confidence factor returns to its original position, and the warning semaphore is reset to 0. Otherwise, the alert status is maintained.

The traditional approach to warning involves classifying the magnitude of mine microseismic energy and taking different response measures based on the classification. However, this paper introduces an early warning strategy that utilizes the matching degree between real-time perceived data points and a model. This strategy demonstrates strong real-time performance and high efficiency.

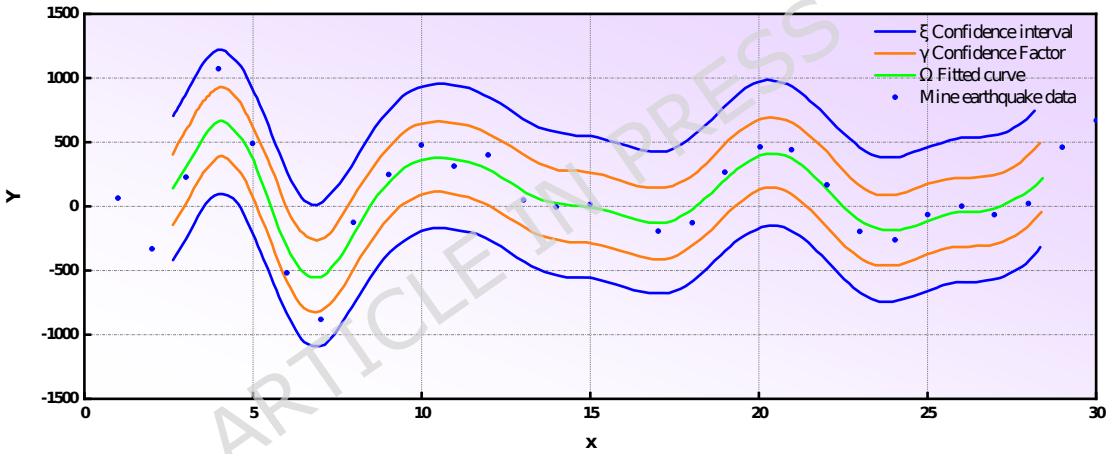

Fig. 6 Schematic diagram of threshold line transformation strategy.

Building upon the transformation rules, a multi-level monitoring and warning method is proposed. The early warning is divided into three stages, namely level 1 to level 3, based on the degree of fit between the perception data and the model. Level 1 warning corresponds to the weakest level of danger and the lowest degree of fit between the perception data and the model. The second level is the intermediate warning, while level 3 corresponds to the most dangerous situation. The triggering rules for the multi-level and hierarchical warning are as follows: When n consecutive perceptual data enter the confidence interval but are outside the confidence factor curve (in accordance with Rule ①), level 1 warning will be

triggered.

① During this period, continuous monitoring of the warning semaphore is conducted. If the warning semaphore is set to 1, the second-level warning will be promptly triggered. Otherwise, the warning will be canceled.

② If n consecutive perceptual data points fall within the confidence interval and also lie within the confidence factor curve (in accordance with rule ②), the level 2 warning will be triggered.

③ At this stage, the monitoring of the warning semaphore continues. If the warning semaphore is set to 1, the Level 3 warning is triggered immediately. Otherwise, the alert level is reduced to level 2.

④ If n consecutive perceptual data points deviate from the confidence interval (following rule 3), all warning levels will be promptly canceled.

The sample size, n, is calculated based on the perceived data, taking into account the sampling frequency of the microseismic sensor and the actual geographical environment of the 8204-2 working face.

4 The application of the early warning model

4.1 The design of a high-frequency microseismic monitoring system

Two functional modules are integrated into the high-frequency microseismic wireless ground station big data monitoring system, namely a primary real-time monitoring module and a secondary data analysis module. Each module is further divided into several sub-modules to provide technical support for its respective main module.The first-level real-time monitoring module is divided into three parts: the data stream conversion processing module, the core magnitude positioning calculation module, and the real-time monitoring visualization module. The secondary data analysis module is divided into two parts: the big data historical data analysis module and the data analysis visualization module. Fig. 7 illustrates the data interaction mode among the system’s modules, where the primary real-time monitoring module realizes real-time acquisition, positioning and

visualization of microseismic data, and the secondary data analysis module conducts in-depth mining and statistical visualization of historical big data, with unidirectional data transmission from the primary module to the secondary module. Once the microseismic correlation calculation is completed, the corresponding microseismic data in the mining area will be automatically transferred to the database of the data center server.

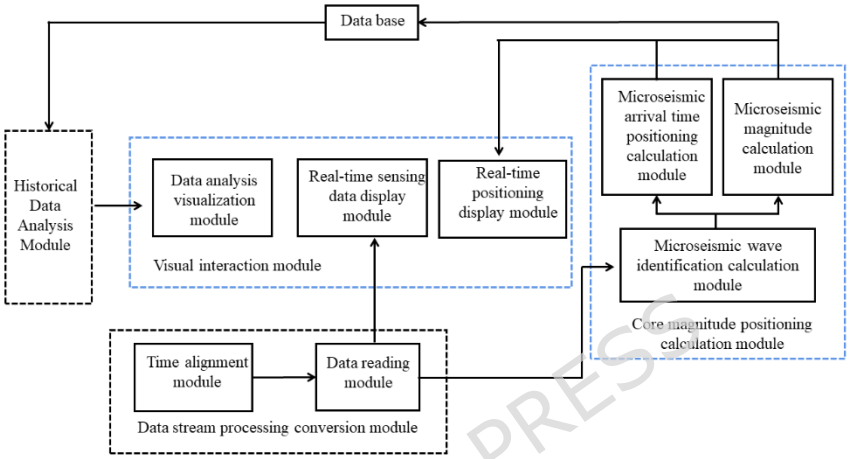

Fig. 7 The data interaction mode among the modules of the system.

Before being written into the database, the source coordinates (x, y) need to be determined. Only when the 15 constraint condition is met, the microseismic data will be stored in the database.

$$\begin{cases} x_{min} \le x \le x_{max} \\ y_{min} \le y \le y_{max} \end{cases} \tag{15}$$

Where, $x_{min}, x_{max}, y_{min}, y_{max}$ is the horizontal and vertical coordinate range of the mining area map. The database table contains a uniquely identified autoincrement primary key id, mine name, triaxial coordinates identifying the source location xData, yData, zData, microseismic occurrence time quackTime and microseismic magnitude quackGrade. After the query page of the front desk sends a data request to the corresponding Servlet, it searches the database through the user's query conditions and returns the results to the front page.

4.2 Analysis of monitoring results of early warning model

Fig. 8 (a) illustrates the setup of a wireless ground station in the 8204-2

working face of the Tashan mining area. A solar power supply system is adopted to power all on-site monitoring equipment. The outdoor hardware equipment is mounted on 5-meter-high metal posts. The 8202-4 working face of Tashan Mine is situated in a mountainous region with no human settlement, power supply, or network infrastructure. The terrain is characterized by significant elevation differences. To overcome these challenges, a total of 7 ground monitoring stations and 11 sets of high-frequency microseismic collectors were strategically selected in Tashan Mine. These devices are interconnected through a local area network (LAN) and can establish seamless communication with the central machine server. In Fig. 8 (b), the parameters of the assembled research center machine and server were fine-tuned to enable independent wide area network (WAN) connectivity for the central machine server.

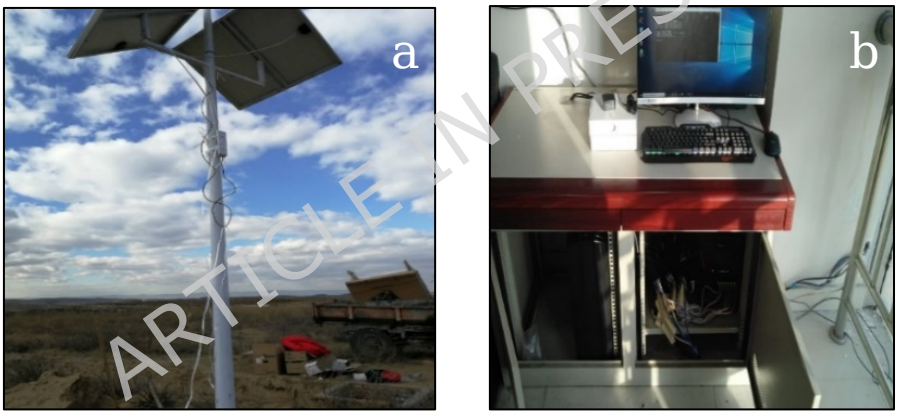

Fig. 8 Commissioning of wireless service center and construction of ground station in mine area.

All 11 sets of high-frequency collector devices, 26 sets of network bridge devices, 2 sets of high-performance routers and switches, and central computer servers have been configured for LAN + WAN interconnection, as follows:

(1) The 11 sets of high-frequency microseismic collector devices are connected to the central machine and server within the LAN. This allows seamless access between the collector and the central machine and server, avoiding any IP address conflicts with the 26 sets of bridge devices. By installing remote access control software and enabling WAN sharing, remote access to individual devices can be

achieved.

(2) The network bridge devices have been configured based on the network bridge configuration parameter table, enabling AP connectivity and convergence connectivity for all 26 sets of devices. This ensures a one-to-one mapping relationship among the network devices. Additionally, all 26 sets of network bridges, 11 sets of high-frequency collector devices, and 2 sets of high-performance router + switch devices are in the same network segment.

(3) The core network access settings for the 2 sets of high-performance routers and switches have been completed. This allows real-time access to the microseismic data from the 11 sets of high-frequency collector devices through data aggregation with the 26 sets of bridge devices. Furthermore, the central machine server is connected to achieve complete network connectivity.

By establishing an ad hoc network in the mining area, unlimited access to the LAN of all ground stations can be achieved. The network connectivity of each ground station and network equipment can be monitored in real time through the visual interface on the central computer server. This enables the determination of the operational status of the high-frequency collector. The study focuses on implementing a two-level microseismic monitoring management mode suitable for the Tashan mine, where a first-level real-time microseismic monitoring system is installed at the central machine for continuous monitoring.

Table 1 Expression methods of microseismic events.

Serial number	Microseismic event energy	Radius	Color representation	Shape representation
1	E<102J	8	Green	
2	102J≤E<103J	10	Yellow	
3	103J≤E<104J	12	Blue	
4	104J≤E<105J	16	Red	
5	Ground microseismic	—	Red	

measurement point

With manual verification method, microseismic events can be efficiently and accurately determined. The second-level big data statistical analysis platform imports the statistical outcome of microseismic events and the historical monitoring data of the whole station into the remote Hadoop big data cluster, researches the multi-level big data linkage query method, and implements the query operation of the statistical results of microseismic events.

Table 2 shows the success rate of microseismic monitoring in Tashan Mine based on the monitoring and warning model in the past 6 months. It can be analyzed from the table that the warning strategy based on the threshold model can well meet the early warning role of microearthquakes, and its success rate of monitoring is greater than or equal to 95%, providing safety guarantee for mining. Based on the microseismic location results, the expression method of microseismic events is shown in Table 1

Table 2 Success rate of mine microseismic monitoring by warning and monitoring system.

Monitoring month	**January**	**February**	**March**	**April**	**May**	**June**
Warning success rate (%)	96.467	95.814	95.142	97.840	97.615	98.737

As illustrated in Fig. 9, microseismic events in the last 6 months are statistically analyzed, and the relation between the degree of the face propulsion and the number of microseismic lunar events and energy is analyzed.

In January 2019, the face advanced 150m (from 730m mined in 2018 to 880m). As illustrated in Fig. 9(a), microseismic events were mainly clustered in two parts. First, three microseismic events above 103 J were detected in the coal pillar region at the junction of 8204-2 working face and 8204 working face, mainly because these coal pillars were subjected to concentrated loads. There are more microseismic events; Second, it is 130 m forward of the face. Therefore, it was judged that the influence span of the mining face ahead is about 130m. It is

suggested to strengthen monitoring during the mining process and take pressure relief measures for the coal pillar at the side of 8204 working face.

In February 2019, the mining face advanced 170 m (from 880m mined in January to 1050m). As illustrated in Fig. 9(b), the coal seam has no obvious faults and other structures, the coal seam occurrence is relatively stable, and microseismic events exhibit a relatively uniform spatial distribution, primarily distributed in the goaf of working face 8204 and 8206, with one event of more than 104 J occurring. 55m away from 8204-2 working face. In March 2019, the mining face advanced 140 m (from 1050m mined in February to 1190m), as shown in Fig. 9(c). After comparison, it is found that there are no obvious faults and other structures in the coal seam, the occurrence of coal seam is relatively stable, and the geographic distribution of microseismic events is more uniform, clustered in the coal pillar area between the working face 8204 and 8204-2. As shown in the figure, there were 5 microseismic events in the coal pillar region, including 1 event above 104J and 3 events above 103J above the roadway of 8204-2 working face.

In April 2019, the working face was progressed 120 m (from 1190m in March to 1310m), as illustrated in Fig. 9(d). During this process, the mining face was widened, the advancing speed was reduced, there were no obvious faults and other structures in the coal seam, the occurrence of coal seam was stable, and the spatial distribution of microseismic events was more uniform, concentrated in the coal pillar region between the working face 8204 and 8204-2. As shown in the figure, there were 6 microseismic events in the coal pillar area, including 3 events above 103J and 2 events between 102J-103J.

In May 2019, the working face advanced 160 m (from 1310m mined in April to 1470m). As shown in Fig. 9(e), there were no obvious faults and other structures in the coal seam during this progression, and the occurrence of coal seam was stable. Of the three microseismic events detected, two possessed energies greater than 10^4 J; the hypocenters for these high-energy events were identified in the

8202 working face goaf. A microseismic event was located in the goaf behind the working face with an energy between 103 J-104 J.

In June 2019, the working face advanced 130 m (from 1470 m to 1600 m mined in May), as shown in Fig. 9(f). During this process, there were no obvious faults and other structures in the coal seam, and the occurrence of coal seam was stable. However, owing to the proximity of the face to the stop-mining line, the number and energy of microseismic events were both high, and 42 microseismic events were detected. There are 4102 J-103 J events, 28103 J-104J events, and 10 events greater than 104 J events.

Microseismic events near the stop-mining line exhibit distinct spatiotemporal features: they cluster in the coal pillar between the 8204 and 8204-2 working faces and the 8204 goaf, with event number and energy rising progressively as the face nears the stop-mining line, and high-energy events concentrated in the final 20 m of advancement. This phenomenon is mainly caused by in-situ, mining-induced and residual stress superposition, abrupt changes in rock mass constraints from the artificial stop-mining boundary, and aggravated rock damage by pre-mining disturbance. The microseismic signals here show a “high frequency + multi-level energy + spatial concentration” response mode, with low-energy events as the background, medium-energy ones as the main body and high-energy ones as key early warning signals, and the signals feature a shortened time domain and increased frequency in time-frequency characteristics.

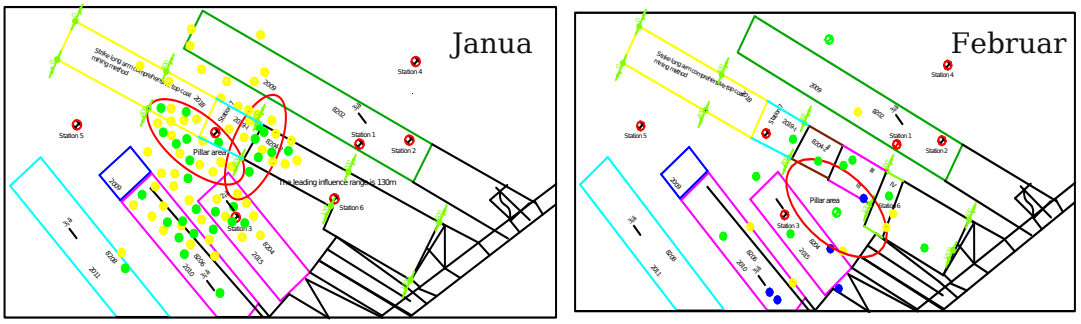

(a) (b)

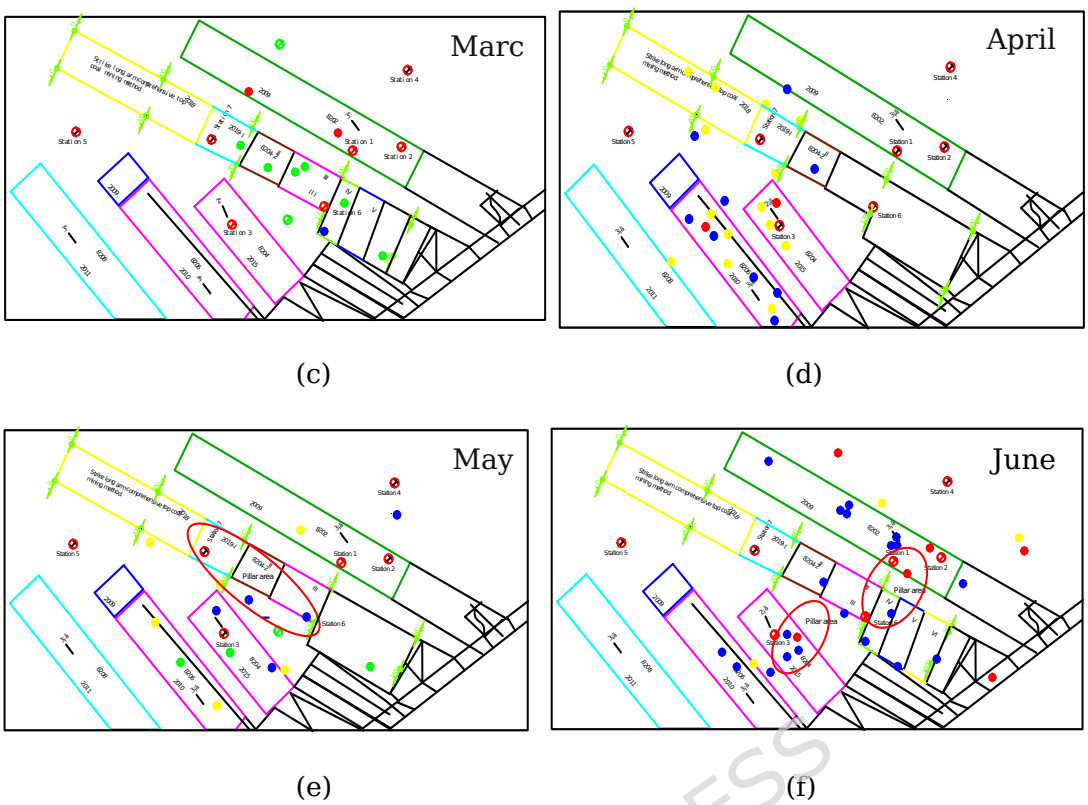

Fig. 9 Results of microseismic monitoring and location in Tashan Mine from January to June

In July 2019, the working face reached the stop-mining line, the working face equipment was withdrawn, and the surface microseismic monitoring equipment was dismantled. In summary, based on the microseismic data of working face 8204-2 in Tashan Mine during the mining period from January to June, 297 microseismic events were accurately located, reaching a combined energy of 7.27 × 105 J, and the working face's influence extended up to approximately 130 m ahead.. Although the working face was an isolated face, effective monitoring and pressure relief measures were adopted. No energy events and dynamic disasters exceeding 105 J occurred during mining.

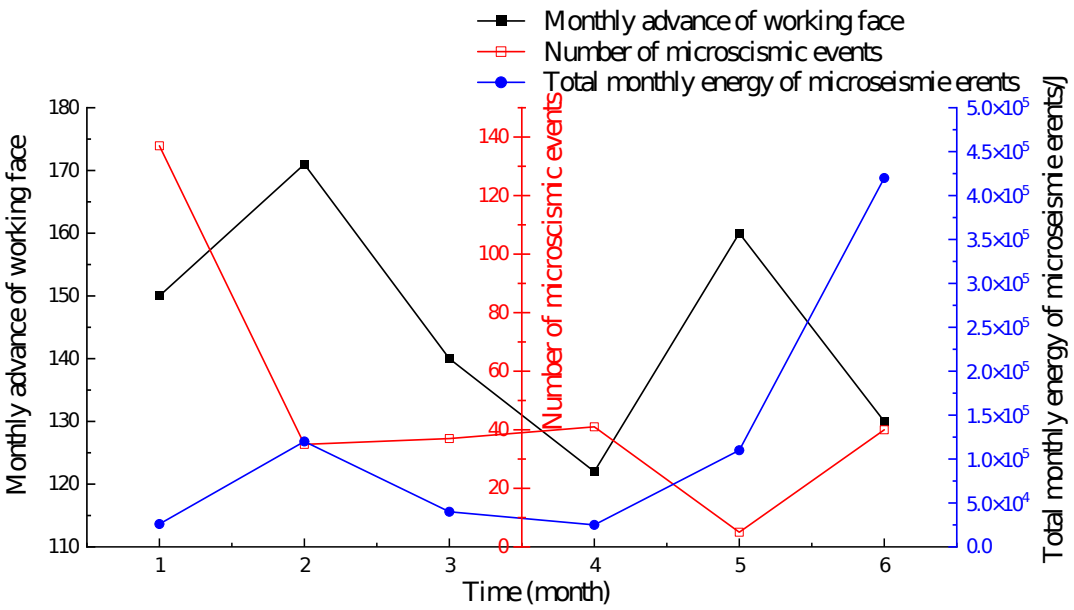

Fig. 10 monthly advance rate of mining face and its relationship with microseismic event count and energy

As illustrated in Fig. 10, overall 297 microseismic events were detected from January to June, reaching a combined energy of 7.27×10^5 J. The working face advanced successively by 150m, 170m, 140m, 120m, 160m, and 130m during this period. Microseismic monitoring recorded 136, 38, 36, 41, 3, and 42 events from January to June, respectively. The corresponding total energy released for each month was 3.44×10^4 J, 1.15×10^5 J, 3.59×10^4 J, 2.43×10^4 J, 2.43×10^4 J, and 4.21×10^5 J, respectively.

The data suggest a nonlinear dependence of microseismic energy release and event frequency on the extent of working face advancement. This nonlinearity essentially reflects the different responses of rock mass strain energy release to mining disturbance intensity: rapid advance leads to concentrated energy release in the form of a small number of high-energy events, while slow advance results in step-by-step release through multiple low-energy microseismic activities. The number of microseismic events decreases With progressive face advance, while it increases with a decrease in advancement. When the working face advanced more, the count of microseismic events in January and February decreased, representing a 234% rise in the cumulative microseismic energy relative to January, as the rock

mass had no sufficient time for slow rupture and accumulated strain energy was released intensively. However, from March to April, with a decrease in advancement, the count of microseismic events increased compared to that of March, while the total energy of microseismic events remained equal. Furthermore, from May to June, as the degree of advancement decreased, with a significant increase observed in the total microseismic energy, by 3.96×10^5 J compared to May, marking a year-on-year increase of 1630 %.

This paper utilizes the complex underground working face geological structure, geographical environment, well group characteristics, and the occurrence rules of dynamic disasters in coal mining to establish the suitable methods for high-frequency microseismic timing determination and dynamic disaster microseismic location in the mining area. Additionally, it investigates the development of a mining area monitoring system that is specifically designed for high-frequency microseismic monitoring in complex environments.

By taking into account the underground mining conditions and geological structure, this study presents future trends in dynamic disaster occurrences and proposes risk warning methods. These findings provide a solid theoretical foundation for ensuring safe mining practices in the mining area. The ultimate aim is to prevent casualties, minimize equipment damage, and reduce both engineering costs and economic losses.

4.3 Precision analysis of traditional mine microseismic signal identification

The precise identification of microseismic signals in traditional mines is usually achieved via spectral analysis and regression analysis, with previous studies also applying spectral transformation, neural networks and Fisher's discriminant method for such analysis (Table 3). Nevertheless, these traditional methods have inherent drawbacks: spectral analysis is seldom used in mining due to its high professional expertise requirement despite its insightful results, and

Fisher's discriminant analysis brings randomness to modeling as its parameter selection depends on non-directional experience, even with good test set identification performance.

In this study, the nonlinear threshold curve model achieves more efficient signal identification and early warning results for the 8204-2 working face of Tashan Mine by optimizing the core logic of traditional methods. It abandons single energy classification for early warning and adopts the matching degree between real-time sensing data and the hazard model, which better conforms to the nonlinear evolution law of microseismic events; it also optimizes signal recognition logic through the combination of wavelet decomposition denoising and feature point extraction to mitigate high-frequency noise interference, and replaces fixed thresholds with dynamic threshold determination based on confidence factor transformation to enhance early warning adaptability. In terms of scenario adaptability, recurrent neural networks and genetic algorithms are suitable for microseismic monitoring in simple, low-noise geological environments, and logistic regression for medium-scale mining areas with distinct microseismic event types, while the proposed model exhibits significant advantages in complex geological environments with high noise interference, soft rock working faces and severe stress concentration, thus being more applicable to dynamic disaster early warning in deep mines.

Table 3 Comparison of traditional microseismic signal identification and early warning accuracy with this research method.

Scholar	Methods or Objects	Accuracy
Muller et al.[33]	Recurrent neural network (RNN)	90%
Orlic and Loncaric[34]	Genetic algorithm	85%
Vallejos and McKinnon[35]	Logistic Regression and neural networks	95%
This Study	Nonlinear Threshold Curve Model	≥95%

5 Conclusions

The study from the characterization of high-frequency the acquisition and

source localization of microseismic signals theory to the design of microseismic signal real-time monitoring in the complex and changeable mining environment, and has a high applicability of equipment. Through the simulation of the historical data of microearthquake disaster and the multi-level monitoring, the potential mining threats can be found and dealt with in time, which brings high value to the social life and production, the main findings of this research are summarized below:

(1) The high-frequency microseismic ground monitoring station is constructed, and the method of determining the microseismic arrival time, microseismic location and microseismic magnitude calculation is proposed. On the basis of this hardware system construction, the secondary management platform of microseismic big data is further constructed, which provides the theoretical framework and system reference for the coal industry to build and promote the development of surface microseismic monitoring. To a certain extent, it fills the gap in the field of big data analysis of domestic coal mine surface microseismic monitoring.

(2) By analyzing the actual situation of Tashan Mine, a mine early-warning method for dynamic hazards utilizing a nonlinear threshold curve model was proposed. The massive historical hazard data were summarized, and the data features were extracted by mobile regression method. On this basis, the coal mine dynamic hazard model was established by linear regression method, which established a theoretical foundation for identifying dynamic hazards in coal mines. By constructing the recognition domain through confidence intervals, the method of confidence factor transformation was proposed to predict the future development trend of hazard waveform, which provided theoretical support for coal mine hazard disaster warning technology.

(3) Early warning was carried out on the matching degree between real-time perceived data points and the model, and the sample size n of perceived data was obtained according to the sampling frequency of microseismic sensors and the

actual geographical environment of 8204-2 working face. According to the fitting degree of perceived data from weak to strong, the early warning was divided into three stages from the first to the third level, and the mining area was monitored in an all-round way in real time to avoid the defects of traditional monitoring methods.

(4) The mine microseismic surveillance and alert system building on the nonlinear threshold curve model was of great contribution to the mining of deep coal seam mining area. Compared with the traditional microseismic signal identification research method, the surveillance and early warning approach in this study has a prediction accuracy higher than 95% and has certain reference value.

The mine microseismic monitoring and early warning system based on the nonlinear threshold curve model proposed in this study has been validated in practice at the 8204-2 working face of Tashan Mine, demonstrating its high accuracy and engineering applicability in complex geological environments. This provides important technical support for the precise prevention and control of dynamic disasters in deep coal mines. In the future, big data and artificial intelligence technologies can be leveraged to continuously optimize the model's adaptive capabilities from three specific research perspectives: first, integrate multi-source mining data based on big data technology to enrich the training dataset of the model; second, introduce LSTM-CNN hybrid neural network to realize adaptive adjustment of threshold curve parameters for complex geological conditions; third, apply transfer learning to the model to expand its generalized application scenarios under different coal seam occurrence conditions and mining processes. This technological system can be widely promoted to various deep mines and underground engineering fields, providing stronger technical support for the safe and efficient development of the coal industry and the management of underground engineering disasters.

Fundings

Supported by the National Natural Science Foundation of China (Grants. 52274206; 52404086).

Supported by State Key Laboratory of Intelligent Construction and Healthy Operation and Maintenance of Deep Underground Engineering（SDGZK2420）

Competing Interests

This study does not have any conflicts of interest with any institutions or individuals in terms of utilization.

Authors' Contributions

The concept and design, Jiaxu Jin; Microseismic disaster early warning model, Jie Liu and Jun Wang; Microseismic monitoring system development, Pengfei Wu; Data collection and dynamic disaster early warning system application analysis Yunlong Mo and Lei Zhang; Writing–original draft, Yong Xiao; Writing–review & editing, Yong Xiao.

Data Availability Statement

The authors confirm that the data supporting the finding of this study are available within the article.

References

[1] Wang, C.; Zhao, X.; Zhu, Q.; Yu, W.; Wu, T. Microseismic Source Location Method and Microseismic Event Source Parameter Characteristic Analysis for Surface Microseismic System. *Mining, Metallurgy & Exploration* **2025**, *42* (5), 2963-2980. DOI: 10.1007/s42461-025-01322-0.

[2] Vafaei Shoushtari, S.; Giroux, B.; Gloaguen, E.; Nasr, M. Detection of mining-induced microseismicity through a deep convolutional neural network. *Journal of Applied Geophysics* **2025**, 106069. DOI: 10.1016/j.jappgeo.2025.106069.

[3] Zhang, X.; Mao, Q.; Yu, R.; Jia, R. A multivariate time series prediction model for microseismic characteristic data in coal mines. *Journal of Applied Geophysics* **2025**, *236*, 105683. DOI: 10.1016/j.jappgeo.2025.105683.

[4] Lai, X.; Jia, C.; Cui, F.; Chen, J.; Zhou, Y.; Feng, G.; Gao, Y. Microseismic energy distribution and impact risk analysis of complex heterogeneous spatial evolution of extra-thick layered strata. *Scientific Reports* **2022**, *12* (1), 10832. DOI: 10.1038/s41598-022-14538-7.

[5] Liu, J.-p.; Si, Y.-t.; Wei, D.-c.; Shi, H.-x.; Wang, R. Developments and prospects of microseismic monitoring technology in underground metal mines in China. *Journal of Central South University* **2021**, *28* (10), 3074-3098. DOI: 10.1007/s11771-021-4839-y.

[6] Cui, F.; Dong, S.; Lai, X.; Chen, J.; Cao, J.; Shan, P. Study on Rule of Overburden Failure and Rock Burst Hazard under Repeated Mining in Fully Mechanized Top-Coal Caving Face with Hard Roof. *Energies* **2019**, *12* (24). DOI: 10.3390/en12244780.

[7] Ge, M. Efficient mine microseismic monitoring. *International Journal of Coal Geology* **2005**, *64* (1-2), 44-56. DOI: 10.1016/j.coal.2005.03.004.

[8] Liang, Z.; Xue, R.; Xu, N.; Li, W. Characterizing rockbursts and analysis on frequency-spectrum evolutionary law of rockburst precursor based on microseismic monitoring. *Tunnelling and Underground Space Technology* **2020**, *105*. DOI: 10.1016/j.tust.2020.103564.

[9] Liu, C.; Xue, J.; Yu, G.; Cheng, X. Fractal characterization for the mining crack evolution process of overlying strata based on microseismic monitoring technology. *International Journal of Mining Science and Technology* **2016**, *26* (2), 295-299. DOI: 10.1016/j.ijmst.2015.12.016.

[10] Ma, T.; Lin, D.; Tang, C. a.; Yadav, K. P.; Feng, Z.; Ma, K. Microseismic Monitoring, Positioning Principle, and Sensor Layout Strategy of Rock Mass Engineering. *Geofluids* **2020**, 1-20. DOI: 10.1155/2020/8810391.

[11] Ma, T.; Lin, D.; Tang, L.; Li, L.; Tang, C. a.; Yadav, K. P.; Jin, W. Characteristics of rockburst and early warning of microseismic monitoring at qinling water tunnel. *Geomatics, Natural Hazards and Risk* **2022**, *13* (1), 1366-1394. DOI:

10.1080/19475705.2022.2073830.

[12] Ma, T.-h.; Tang, C.-a.; Liu, F.; Zhang, S.-c.; Feng, Z.-q. Microseismic monitoring, analysis and early warning of rockburst. *Geomatics, Natural Hazards and Risk* **2021**, *12* (1), 2956-2983. DOI: 10.1080/19475705.2021.1968961.

[13] Ma, T.-H.; Tang, C.-A.; Tang, S.-B.; Kuang, L.; Yu, Q.; Kong, D.-Q.; Zhu, X. Rockburst mechanism and prediction based on microseismic monitoring. *International Journal of Rock Mechanics and Mining Sciences* **2018**, *110*, 177-188. DOI: 10.1016/j.ijrmms.2018.07.016.

[14] Dong, L.-j.; Li, X.-b.; Peng, K. Prediction of rockburst classification using Random Forest. *Transactions of Nonferrous Metals Society of China* **2013**, *23* (2), 472-477. DOI: 10.1016/s1003-6326(13)62487-5.

[15] Ding, L.; Chen, Z.; Pan, Y.; Song, B. Mine Microseismic Time Series Data Integrated Classification Based on Improved Wavelet Decomposition and ELM. *Cognitive Computation* **2022**, *14* (4), 1526-1546. DOI: 10.1007/s12559-022-09997-z.

[16] Jiang, W.; Ding, W.; Zhu, X.; Hou, F. A Recognition Algorithm of Seismic Signals Based on Wavelet Analysis. *Journal of Marine Science and Engineering* **2022**, *10* (8). DOI: 10.3390/jmse10081093.

[17] Zhang, J.; Jiang, R.; Li, B.; Xu, N. An automatic recognition method of microseismic signals based on EEMD-SVD and ELM. *Computers & Geosciences* **2019**, *133*. DOI: 10.1016/j.cageo.2019.104318.

[18] Zhang, X.; Zhao, Z.; Jia, R.; Cao, L. Identification of Microseismic Signals Based on Multiscale Singular Spectrum Entropy. *Shock and Vibration* **2020**, *2020*, 1-12. DOI: 10.1155/2020/6717128.

[19] Peng, K.; Tang, Z.; Dong, L.; Sun, D. achine Learning Based Identification of Microseismic Signals Using Characteristic Parameters. *Sensors* **2021**, *21* (21). DOI: 10.3390/s21216967.

[20] Li, Q.; Li, Y.; He, Q. Mine-Microseismic-Signal Recognition Based on LMD–PNN Method. *Applied Sciences* **2022**, *12* (11). DOI: 10.3390/app12115509.

[21] Zhang, Z.-b.; Sun, J.; Zhang, H.-t. Nonlinear evolution characteristics of the mutual-exciting network of acoustic emission events and the multifractal early warning model. *Fractals*, **2026**: 2650033. DOI: 10.1142/S0218348X26500337.

[22] He, S.; Qin, M.; Qiu, L.; Song, D.; Zhang, X. Early warning of coal dynamic disaster by precursor of AE and EMR "quiet period". *International Journal of Coal Science & Technology* **2022**, *9* (1). DOI: 10.1007/s40789-022-00514-z.

[23] Jiskani, I. M.; Ullah, B.; Shah, K. S.; Bacha, S.; Shahani, N. M.; Ali, M.; Maqbool, A.; Qureshi, A. R. Overcoming mine safety crisis in Pakistan: An appraisal. *Process Safety Progress* **2019**, *38* (4). DOI: 10.1002/prs.12041.

[24] Huo, Y.; Zhang, W.; Zhang, J.; Yang, H. Using microseismic events to improve the accuracy of sensor orientation for downhole microseismic monitoring. *Geophysical Prospecting* **2021**, *69* (6), 1167-1180. DOI: 10.1111/1365-2478.13099.

[25] Dou, L.; Cai, W.; Cao, A.; Guo, W. Comprehensive early warning of rock burst utilizing microseismic multi-parameter indices. *International Journal of Mining Science and Technology* **2018**, *28* (5), 767-774. DOI: 10.1016/j.ijmst.2018.08.007.

[26] Yu, Q.; Zhao, D.; Xia, Y.; Jin, S.; Zheng, J.; Meng, Q.; Mu, C.; Zhao, J. Multivariate Early Warning Method for Rockburst Monitoring Based on Microseismic Activity Characteristics. *Frontiers in Earth Science* **2022**, *10*. DOI: 10.3389/feart.2022.837333.

[27] Wang, X.; Liu, W.; Jiang, X.; Zhang, Q.; Wei, Y. Evolution Characteristics of Overburden Instability and Failure under Deep Complex Mining Conditions. *Geofluids* **2022**, *2022*, 1-16. DOI: 10.1155/2022/6418082.

[28] Xia, X.; Chen, Z.; Wei, W. Research on Monitoring and Prewarning System of Accident in the Coal Mine Based on Big Data. *Scientific Programming* **2018**,

2018, 1-10. DOI: 10.1155/2018/9308742.

[29] Shi, Y.; Zhang, D.; Ji, H.; Dai, R.; Wu, Y.; Wang, B. A Study on Enhancing the Accuracy of P Wave Detection based on Double-Filtering Algorithm for Microseismic Signals from Underground Mines. *IOP Conference Series: Earth and Environmental Science* **2020**, *440* (5). DOI: 10.1088/1755-1315/440/5/052095.

[30] Wei, H.; Shu, W.; Dong, L.; Huang, Z.; Sun, D. A Waveform Image Method for Discriminating Micro-Seismic Events and Blasts in Underground Mines. *Sensors* **2020**, *20* (15). DOI: 10.3390/s20154322.

[31] Niu, D.; Diao, L.; Zang, Z.; Che, H.; Zhang, T.; Chen, X. A Machine-Learning Approach Combining Wavelet Packet Denoising with Catboost for Weather Forecasting. *Atmosphere* **2021**, *12* (12). DOI: 10.3390/atmos12121618.

[32] Huang, G.-B.; Zhu, Q.-Y.; Siew, C.-K. Extreme learning machine: Theory and applications. *Neurocomputing* **2006**, *70* (1-3), 489-501. DOI: 10.1016/j.neucom.2005.12.126.

[33] Curilem, M.; Vergara, J.; Martin, C. S.; Fuentealba, G.; Cardona, C.; Huenupan, F.; Chacón, M.; Salman Khan, M.; Hussein, W.; Yoma, N. B. Pattern recognition applied to seismic signals of the Llaima volcano (Chile): An analysis of the events' features. *Journal of Volcanology and Geothermal Research* **2014**, *282*, 134-147. DOI: 10.1016/j.jvolgeores.2014.06.004.

[34] Orlic, N.; Loncaric, S. Earthquake—explosion discrimination using genetic algorithm-based boosting approach. *Computers & Geosciences* **2010**, *36* (2), 179-185. DOI: 10.1016/j.cageo.2009.05.006.

[35] Vallejos, J. A.; McKinnon, S. D. Logistic regression and neural network classification of seismic records. *International Journal of Rock Mechanics and Mining Sciences* **2013**, *62*, 86-95. DOI: 10.1016/j.ijrmms.2013.04.005.